J. Plasma Phys. (2017), *vol.* 83, 705830103 © Cambridge University Press 2017
doi:10.1017/S0022377816001264

A pressure tensor description for the time-resonant Weibel instability

M. Sarrat[1],†, D. Del Sarto[1] and A. Ghizzo[1]

[1]Institut Jean Lamour, UMR 7198 CNRS – Université de Lorraine, F-54506 Vandoeuvre-lès-Nancy, France

(Received 30 September 2016; revised 20 December 2016; accepted 20 December 2016)

We discuss a fluid model with inclusion of the complete pressure tensor dynamics for the description of Weibel-type instabilities in a counterstreaming beam configuration. Differently from the case recently studied in Sarrat *et al.* (*Europhys. Lett.*, vol. 115, 2016, 45001), where perturbations perpendicular to the beams were considered, here we focus only on modes propagating along the beams. Such a configuration is responsible for the growth of two kinds of instabilities, the two-stream instability and the Weibel instability, which in this geometry becomes 'time resonant', i.e. propagating. This fluid description agrees with the kinetic one and makes it possible e.g. to identify the transition between non-propagating and propagating Weibel modes, already evidenced by Lazar *et al.* (*J. Plasma Phys.*, vol. 76 (1), 2010, p. 49) as a 'slope breaking' of the growth rate, in terms of a merger of two non-propagating Weibel modes.

Key words: astrophysical plasmas, plasma instabilities, space plasma physics

1. Introduction

Velocity-space anisotropy-driven instabilities capable of generating strong quasi-static magnetic fields are frequent in many frameworks of plasma physics, ranging from astrophysical plasmas to laboratory laser–plasma interactions. Expressions such as 'Weibel-type' or 'Weibel-like' are frequently used as generic names for these instabilities. Examples are the pure Weibel instability (WI) driven by a temperature anisotropy (Weibel 1959) or beam–plasma instabilities like the current filamentation instability (CFI), generated by a linear momentum anisotropy (Fried 1959). The latter usually requires a perturbation with a wave vector orthogonal to the beams. However, beam–plasma systems, in nature, are more generally destabilised by oblique (with respect to the beams) wave vectors, so that classical Weibel instabilities are often in competition with the electrostatic two-stream instability (TSI) or the oblique instability (Bret, Firpo & Deutsch 2005; Bret, Gremillet & Dieckmann 2010) depending on the symmetry properties of the beams and on their velocity (relativistic or not). Therefore, the family of Weibel-type instabilities includes also phenomena resulting from the combination of these two types of velocity anisotropies, such as the Weibel–CFI coupled modes or the time-resonant Weibel instability (TRWI). The latter, investigated

† Email address for correspondence: mathieu.sarrat@univ-lorraine.fr

https://doi.org/10.1017/S0022377816001264 Published online by Cambridge University Press

in Lazar *et al.* (2009), Lazar, Dieckmann & Poedts (2010) and Ghorbanalilu *et al.* (2014), is triggered by an excess of thermal energy perpendicular to the direction of the electron beams and is a time resonant, i.e. propagating instability. At relativistic speeds, the oblique and CFI instabilities are dominant (Bret *et al.* 2010), whereas in the non-relativistic regime the TRWI grows faster than the TSI (Lazar *et al.* 2009), the oblique and the CFI.

In this article we focus on configurations with perturbations propagating along the beams, so that only the TRWI and the TSI can be excited. This simplification is a preliminary step to next applying the fluid model, including a full pressure tensor dynamics, first investigated by Basu (2002) and Sarrat, Del Sarto & Ghizzo (2016) for wave vectors perpendicular to the beams, to the case of perturbations with generic oblique propagation. These modes affect the stability and the dynamics of (counterstreaming) electron beams, which in the non-relativistic regimes can be generated, e.g. in the nonlinear stage of three-wave parametric decays, such as Raman-type instabilities in laser–plasma interactions (Masson-Laborde *et al.* 2010). In stimulated Raman scattering as well as in self-focusing processes, indeed, Vlasov (Ghizzo, Huot & Bertrand 2003; Ghizzo *et al.* 2007) and Particle-In-Cell (PIC) (Denavit 1992; Guérin *et al.* 1996) simulations evidence kinetic heating processes which are anisotropic along or perpendicular to the electromagnetic wave propagation direction. Estimating that relativistic effects become quantitatively important when electron kinetic energy is comparable to (or stronger than) their rest energy $mc^2 \sim 511$ keV, m and c being respectively the electron mass and the speed of light in the vacuum (see e.g. Lazar *et al.* 2009), a non-relativistic description of Weibel modes may be, at least qualitatively, of interest even to moderately relativistic interpenetrating intergalactic plasmas. The future extension of this model to relativistic regimes will allow broader applications to both astrophysics and high-intensity laser–plasma interactions (Medvedev & Loeb 1999; Schlickeiser & Shukla 2003; Bret *et al.* 2014).

A complete description of these Weibel-type instabilities requires the use of kinetic theory. Nevertheless, fluid model has demonstrated the ability to identify and understand some of their main features. Fried (1959) gave a fluid picture of the pure WI, introducing the concept of CFI: the electron temperature anisotropy is replaced by a momentum anisotropy of two counterstreaming electron beams and the strong anisotropy limit of Weibel's kinetic dispersion relation is then recovered, setting up an analogy between these two driving mechanisms. This approach opened the way to the use of cold fluid models in order to study the linear phase of the relativistic and non-relativistic CFI (Pegoraro *et al.* 1996), possibly in presence of spatial resonances effects (Califano, Pegoraro & Bulanov 1997; Califano *et al.* 1998), and some features of its nonlinear dynamics such as the onset of secondary magnetic reconnection processes (Califano *et al.* 2001), or the coupling with the TSI in a three-dimensional, spatially inhomogeneous configuration (Califano, Del Sarto & Pegoraro 2006).

These cold models are unable to reproduce important results derived from a full kinetic treatment, for example the partially electrostatic behaviour of the CFI when the beams have unequal temperatures (Tzoufras *et al.* 2006; Bret, Gremillet & Bellido 2007). Reduced kinetic models, instead, such as those based on the evolution of waterbag or multistream distributions (Inglebert *et al.* 2012), successfully describe these kinetic features. The multistream model, in particular, deals with Fried's analogy in depth by sampling the distribution function with a bunch of parallel beams, taking advantage of the potential cyclic variables of the problem (Inglebert *et al.* 2011; Ghizzo & Bertrand 2013; Ghizzo, Sarrat & Del Sarto 2016).

https://doi.org/10.1017/S0022377816001264 Published online by Cambridge University Press

The fluid model we here consider, extended to include the full pressure tensor dynamics, can be compared to a reduced kinetic model. The possibility of using such a model in order to investigate Weibel instabilities was first addressed by Basu (2002), who recovered the hydrodynamic limit of the pure WI kinetic dispersion relation. This description has been recently generalised to the thermal CFI and WI–CFI modes in a system of counterstreaming beams (Sarrat *et al.* 2016), and it is here applied to study the onset of the TRWI. Besides resulting consistent with the kinetic description, this fluid analysis allows us to characterise the transition between time-resonant and non-time-resonant regimes of the instability and makes possible the identification of a second, although non-dominant, unstable branch. The purpose of this article is to discuss these points by evidencing the consistency between the full kinetic and this extended fluid description, and the usefulness of the latter in highlighting some features otherwise more difficult to recognise in a full kinetic setting.

The paper is structured as follows. In § 2, we present the model equations and the equilibrium configuration. In § 3, we perform a linear analysis for waves propagating along the beams and obtain the corresponding dispersion matrix. In § 4, we identify the hydrodynamic limit for which both the fluid and kinetic approaches are strictly equivalent. In this limit, we put in evidence the TRWI regime. In § 5 we detail the analysis of the fluid dispersion relation and use it to isolate some kinds of behaviour of the TRWI and to characterise the transition between the resonant and the non-resonant regimes.

2. The fluid model

2.1. *Model equations*

We consider two non-relativistic counterstreaming electron beams ($\alpha = 1, 2$) in a hydrogen plasma at time scales $\Delta t \lesssim \omega_{pi}^{-1}$, where ω_{pi} is the ion plasma frequency. Consequently, the ions form a neutralizing equilibrium background, with a uniform and constant density n_i, whose dynamics will be neglected in the following. We write the first three moments of Vlasov equation for each beam (see e.g. Del Sarto, Pegoraro & Tenerani 2017):

$$\frac{\partial n_\alpha}{\partial t} + \boldsymbol{\nabla} \cdot (n_\alpha \boldsymbol{u}_\alpha) = 0, \tag{2.1}$$

$$\frac{\partial \boldsymbol{u}_\alpha}{\partial t} + \boldsymbol{u}_\alpha \cdot \boldsymbol{\nabla} \boldsymbol{u}_\alpha = -\frac{e}{m}(\boldsymbol{E} + \boldsymbol{u}_\alpha \times \boldsymbol{B}) - \frac{\boldsymbol{\nabla} \cdot \boldsymbol{\Pi}_\alpha}{m n_\alpha}, \tag{2.2}$$

$$\begin{aligned} &\frac{\partial \boldsymbol{\Pi}_\alpha}{\partial t} + \boldsymbol{\nabla} \cdot (\boldsymbol{u}_\alpha \boldsymbol{\Pi}_\alpha) + \boldsymbol{\nabla} \boldsymbol{u}_\alpha \cdot \boldsymbol{\Pi}_\alpha + (\boldsymbol{\nabla} \boldsymbol{u}_\alpha \cdot \boldsymbol{\Pi}_\alpha)^{\mathrm{T}} \\ &\quad = -\frac{e}{m}(\boldsymbol{\Pi}_\alpha \times \boldsymbol{B} + (\boldsymbol{\Pi}_\alpha \times \boldsymbol{B})^{\mathrm{T}}) - \boldsymbol{\nabla} \cdot \boldsymbol{Q}_\alpha, \end{aligned} \tag{2.3}$$

where apex 'T' expresses matrix transpose. We define the pressure tensor $\boldsymbol{\Pi}_\alpha \equiv n_\alpha m(\langle \boldsymbol{v}\boldsymbol{v} \rangle_\alpha - \boldsymbol{u}_\alpha \boldsymbol{u}_\alpha)$ and the heat flux tensor $\boldsymbol{Q}_\alpha \equiv m n_\alpha \langle (\boldsymbol{v} - \boldsymbol{u}_\alpha)(\boldsymbol{v} - \boldsymbol{u}_\alpha)(\boldsymbol{v} - \boldsymbol{u}_\alpha) \rangle_\alpha$. The notation $\langle \cdots \rangle_\alpha$ indicates average in the velocity coordinate $\boldsymbol{v}$ with respect to the particle distribution function $f_\alpha(\boldsymbol{x}, \boldsymbol{v})$.

These equations are coupled to the Maxwell equations:

$$\boldsymbol{\nabla} \times \boldsymbol{E} + \frac{\partial \boldsymbol{B}}{\partial t} = 0, \quad \boldsymbol{\nabla} \times \boldsymbol{B} = \mu_0 \boldsymbol{J} + \frac{1}{c^2}\frac{\partial \boldsymbol{E}}{\partial t}, \tag{2.4a,b}$$

https://doi.org/10.1017/S0022377816001264 Published online by Cambridge University Press

$$\boldsymbol{\nabla}\cdot\boldsymbol{B}=0, \quad \boldsymbol{\nabla}\cdot\boldsymbol{E}=\frac{\rho}{\epsilon_0}, \tag{2.5a,b}$$

where $\boldsymbol{J}=-e\sum_\alpha n_\alpha \boldsymbol{u_\alpha}$ is the total electron current density and ρ is the total charge density. The latter is related to the particle densities by $\rho=e(n_i-\sum_\alpha n_\alpha)$, where n_i is the ion density and n_α is the α-beam electron density.

Equation (2.3) requires some closure condition on the heat flux, which we choose as $\boldsymbol{\nabla}\cdot\boldsymbol{Q_\alpha}=0$. The consistency of this choice will be shown next, by comparison with the kinetic results. On the other hand, the negligible character of $\boldsymbol{\nabla}\cdot\boldsymbol{Q_\alpha}$ in the fluid description of the pure WI has already been shown to be accurate for a wide range of wavenumbers (Sarrat *et al.* 2016).

2.2. *Equilibrium configuration*

At equilibrium, we suppose the beams are along the y-axis and are represented by their own set of fluid variables: density $n_\alpha^{(0)}$, fluid velocity $\boldsymbol{u}_\alpha^{(0)}=u_{y,\alpha}^{(0)}\boldsymbol{e}_y$ and pressure tensor $\boldsymbol{\Pi}_\alpha^{(0)}$. These quantities are potentially different for each beam. Equilibrium velocities and density are constrained in order to avoid equilibrium electromagnetic fields: quasi-neutrality is ensured by $\sum_\alpha n_\alpha^{(0)}=n_i=n^{(0)}$ and the total electron current is set to zero, that is $\sum_\alpha n_\alpha^{(0)}u_{\alpha,y}^{(0)}=0$. We define the squared plasma frequencies for each beam at equilibrium and for the complete electron system by:

$$\omega_{pe,\alpha}^2\equiv\frac{n_\alpha^{(0)}e^2}{m\epsilon_0}, \quad \omega_{pe}^2\equiv\omega_{pe,1}^2+\omega_{pe,2}^2=\frac{c^2}{d_e^2}, \tag{2.6a,b}$$

with d_e the electron skin depth.

The initial pressure tensor is assumed to be anisotropic for each beam. Similar anisotropic pressure configurations, although generally non-uniform in space, are evidenced by both direct satellite measurements and kinetic simulations of the solar wind turbulence (see for example Servidio *et al.* (2012, 2015), Franci *et al.* (2016)) or magnetic reconnection (see for example Scudder & Daughton (2008), Scudder *et al.* (2012), Scudder (2016)). Even if the mechanism of temperature anisotropisation in each context is still a matter of investigation, the dynamical action of the fluid strain on the pressure tensor components, recently identified as a possible *ab initio* source of non-gyrotropic anisotropy (Del Sarto, Pegoraro & Califano 2016), seems to be a good candidate to explain temperature anisotropies measured, for example, in kinetic turbulence, such as that encountered in the solar wind plasma (Franci *et al.* 2016; Parashar & Matthaeus 2016). Regardless of the mechanism of generation of the initial anisotropy, here we assume an initial anisotropic pressure configuration which is unstable to Weibel-type modes. We make the further simplification of assuming the initial plasma to be homogeneous, in order to neglect spatial resonance effects which are known to determine a localisation of the generated magnetic field (Califano *et al.* 1997, 1998, 2006). While in the most general configuration we should in principle account for a generic orientation of the principal axes of the pressure tensor with respect to the direction of the beams and of the perturbation wave vector, we restrict ourselves to the particular choice of having one of the principal axes of each pressure tensor aligned to the beam direction,

$$\boldsymbol{\Pi}_\alpha^{(0)}=\begin{bmatrix}\Pi_{xx,\alpha}^{(0)} & 0 & 0\\ 0 & \Pi_{yy,\alpha}^{(0)} & 0\\ 0 & 0 & \Pi_{zz,\alpha}^{(0)}\end{bmatrix}, \tag{2.7}$$

https://doi.org/10.1017/S0022377816001264 Published online by Cambridge University Press

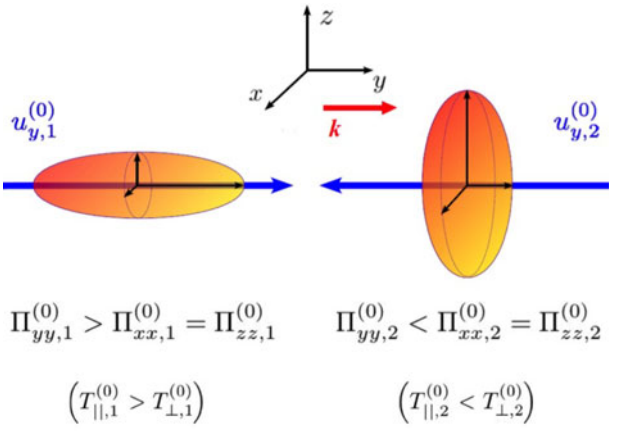


FIGURE 1. Two asymmetrical and counterstreaming beams perturbed by a wave propagating along them. Each beam presents an initial pressure anisotropy between parallel ($\|$) and perpendicular ($\perp$) – to the wave vector – components. In the limit of vanishing initial velocities, $u^{(0)}_{y,1} = u^{(0)}_{y,2} = 0$, as the pure WI requires an excess of perpendicular thermal energy, the population (1) would be stable to a pure Weibel Instability whereas the population (2) would be unstable.

and, for notation purposes which will appear more evident later, we introduce the squared velocities:

$$c^2_{x,\alpha} \equiv \frac{\Pi^{(0)}_{xx,\alpha}}{mn^{(0)}_\alpha}, \quad c^2_{y,\alpha} \equiv \frac{\Pi^{(0)}_{yy,\alpha}}{mn^{(0)}_\alpha}, \quad c^2_{z,\alpha} \equiv \frac{\Pi^{(0)}_{zz,\alpha}}{mn^{(0)}_\alpha}. \tag{2.8a–c}$$

The reason for this geometry choice is that we want to focus here on perturbations propagating along the beams (see figure 1),

$$\boldsymbol{k} = k_y \boldsymbol{e}_y, \tag{2.9}$$

in order to separately describe the TSI and the TRWI (Lazar *et al.* 2010), which in this configuration are decoupled and linearly evolve independently (cf. comments at the end of § 3.2). From a physical point of view, the configuration (2.7) is representative of the anisotropisation, due to kinetic heating and particle trapping processes, which is observed in kinetic simulations of laser–plasma interactions for Stimulated Raman Scattering (SRS) (Ghizzo *et al.* 2006; Albrecht-Marc *et al.* 2007; Ghizzo, Del Sarto & Réveillé 2009; Masson-Laborde *et al.* 2010) or for self-focussing processes (Ghizzo *et al.* 2003, 2007). In these phenomena the symmetry of the system in both the coordinate and velocity space is essentially determined by the direction of propagation of the incident electromagnetic wave. The latter, indeed, turns out to determine also the orientation of the principal axes of the pressure tensor, as the kinetic heating processes related to particle acceleration and trapping occur differently along or perpendicular to the wave vector direction. For instance, the geometry defined in figure 1 can be relevant to the self-induced transparency scenario of a high-intensity laser pulse, i.e. the laser propagation through an overdense plasma in which the propagation is classically forbidden. A significant fraction of the incident

https://doi.org/10.1017/S0022377816001264 Published online by Cambridge University Press

laser energy flux is then converted into electron thermal longitudinal motion during the penetration phase allowed by relativistic effects. Numerical simulations using Vlasov codes in Ghizzo *et al.* (2007) or PIC codes in Guérin *et al.* (1996) have shown that, during the propagation of the laser pulse, a relativistic Doppler shift takes place at the moving wave front and causes the beating of the incoming pump wave with its reflected Doppler-shifted electromagnetic wave (the wave front playing the role of a propagating mirror). However, in the dense plasma, important shielding effects arise and the hot electron current produced by the beating of electromagnetic waves is neutralised by a cold electron return current, as already indicated in Sentoku *et al.* (2003) and Zheng, He & Zhu (2005). The longitudinal hot electron current is then counteracted significantly by a cold return current in the opposite direction and torn into filaments due to the joint interaction of transverse Weibel-type and filamentary instabilities. Thus, the plasma becomes underdense beyond the wave front and the hot electron current propagating in plasma becomes filamentary, being related to the generation of a strong magnetic field. A similar kinetic heating mechanism can be met also in non-relativistic regimes, such as e.g. in three-wave parametric decays (the SRS example quoted above).

Independently from these applications relevant to laser–plasma experiments, and despite being relatively reductive with respect to the most general case, the beam anisotropy described by (2.7) has been largely studied to address the problem of generation of magnetic fields, e.g. on a cosmological scale due to the collision of counterstreaming intergalactic plasmas, and in this configuration the competition between TSI and CFI or TRWI modes has been discussed in both the non-relativistic and relativistic regimes (Lazar, Schlickeiser & Shukla 2006; Lazar 2008; Stockem & Lazar 2008; Stockem *et al.* 2008; Lazar *et al.* 2009, 2010). Moreover, it represents a first generalisation to account for temperature anisotropy effects in the CFI occuring in collisionless shocks like gamma-ray bursts (see, e.g. Medvedev & Loeb 1999). The analysis performed in this configuration is also a first step for the inclusion of a magnetic field along the beam axis, e.g. to study beam instabilities in the solar wind, for which an initial pressure tensor like (2.7) with $\Pi^{(0)}_{xx,\alpha} = \Pi^{(0)}_{zz,\alpha}$ is quite reasonable when the spherical expansion of the solar wind is accounted for in a double-adiabatic framework (Matteini *et al.* 2011).

Therefore, leaving to a future work the discussion of the linear coupling between electrostatic and electromagnetic modes that would arise, even for perturbations purely parallel to the beams (2.9), when a generically oriented pressure tensor is considered, we restrict ourselves to analysing in this extended fluid framework the onset of the TRWI under the hypothesis (2.7), which can be related to a three Maxwellian particle distribution with kinetic temperatures $k_B T_{i,\alpha} \equiv \Pi^{(0)}_{ii,\alpha}/n^{(0)}_{\alpha}$ for $i = x, y, z$,

$$f^{(0)} = n_0 \prod_{i=x}^{z} \left(\frac{m}{2\pi k_B T_i}\right)^{1/2} \exp\left(-\frac{m v_i^2}{2 k_B T_i}\right) = n_0 \prod_{i=x}^{z} \frac{1}{\sqrt{2\pi} c_{i,\alpha}} \exp\left(-\frac{v_i^2}{2 c_{i,\alpha}^2}\right). \quad (2.10)$$

As it is well known, this initial configuration is unstable because of two kinds of anisotropy: one in pressure ($\Pi^{(0)}_{xx,\alpha} \neq \Pi^{(0)}_{yy,\alpha} \neq \Pi^{(0)}_{zz,\alpha}$), the other in momentum (i.e. the counterstreaming beams configuration). The first one triggers the pure WI when the thermal spread transverse to a wave vector $\boldsymbol{k}$ is greater than the one in the parallel direction. The second one generates instability whatever the wave vector orientation, due to the natural repulsion between two counterstreaming electric currents. A perturbation orthogonal to the flow triggers the CFI whereas a perturbation along the flow is responsible for the TSI. A slanting perturbation gives birth to the so-called

https://doi.org/10.1017/S0022377816001264 Published online by Cambridge University Press

oblique modes. The CFI configuration has been widely examined, in particular the coupling between the CFI and the pure WI modes. This coupling has been investigated from a kinetic point of view by Lazar *et al.* (2006, 2009), Stockem & Lazar (2008) in the non-relativistic context, by Bret *et al.* (2010) in the relativistic one and using the non-relativistic fluid pressure tensor description by Sarrat *et al.* (2016).

3. Dispersion matrix

We perturb the equilibrium with Fourier modes $\propto\exp[-\mathrm{i}(\omega t - k_y y)]$, where we define the complex frequency $\omega \equiv \omega_r + \mathrm{i}\gamma$, consisting of a real, propagating part, ω_r, and of a growth (or damping) rate, γ.

3.1. *Linearisation*

Starting with the continuity equation (2.1), we write

$$n_\alpha^{(1)} = n_\alpha^{(0)} \frac{k_y u_{y,\alpha}^{(1)}}{w_\alpha}, \tag{3.1}$$

where we introduce the notation

$$w_\alpha \equiv \omega - \boldsymbol{k}\cdot\boldsymbol{u}_\alpha^{(0)} = \omega - k_y u_{y,\alpha}^{(0)}. \tag{3.2}$$

In a vector form, the linear momentum balance writes

$$u_{x,\alpha}^{(1)} = -\frac{\mathrm{i}e}{mw_\alpha}(E_x^{(1)} + u_{y,\alpha}^{(0)} B_z^{(1)}) + \frac{k_y}{w_\alpha}\frac{\Pi_{xy,\alpha}^{(1)}}{mn_\alpha^{(0)}}, \tag{3.3}$$

$$u_{y,\alpha}^{(1)} = -\frac{\mathrm{i}e}{mw_\alpha}E_y^{(1)} + \frac{k_y}{w_\alpha}\frac{\Pi_{yy,\alpha}^{(1)}}{mn_\alpha^{(0)}}, \tag{3.4}$$

$$u_{z,\alpha}^{(1)} = -\frac{\mathrm{i}e}{mw_\alpha}(E_z^{(1)} - u_{y,\alpha}^{(0)} B_x^{(1)}) + \frac{k_y}{w_\alpha}\frac{\Pi_{yz,\alpha}^{(1)}}{mn_\alpha^{(0)}}, \tag{3.5}$$

with the following expressions for the diagonal components of $\boldsymbol{\Pi}_\alpha^{(1)}$ (cf. (2.3)),

$$\Pi_{xx,\alpha}^{(1)} = \frac{k_y}{w_\alpha}\Pi_{xx,\alpha}^{(0)} u_{y,\alpha}^{(1)}, \quad \Pi_{zz,\alpha}^{(1)} = \frac{k_y}{w_\alpha}\Pi_{zz,\alpha}^{(0)} u_{y,\alpha}^{(1)}, \tag{3.6a,b}$$

$$\Pi_{yy,\alpha}^{(1)} = 3\frac{k_y}{w_\alpha}\Pi_{yy,\alpha}^{(0)} u_{y,\alpha}^{(1)}, \tag{3.7}$$

and for the non-diagonal components,

$$\Pi_{xz,\alpha}^{(1)} = 0, \tag{3.8}$$

$$\Pi_{xy,\alpha}^{(1)} = \frac{k_y}{w_\alpha}\Pi_{yy,\alpha}^{(0)} u_{x,\alpha}^{(1)} - \frac{\mathrm{i}e}{m}\frac{\Pi_{yy,\alpha}^{(0)} - \Pi_{xx,\alpha}^{(0)}}{w_\alpha} B_z^{(1)}, \tag{3.9}$$

$$\Pi_{yz,\alpha}^{(1)} = \frac{k_y}{w_\alpha}\Pi_{yy,\alpha}^{(0)} u_{z,\alpha}^{(1)} - \frac{\mathrm{i}e}{m}\frac{\Pi_{zz,\alpha}^{(0)} - \Pi_{yy,\alpha}^{(0)}}{w_\alpha} B_x^{(1)}. \tag{3.10}$$

The Maxwell–Faraday equation allows us to eliminate the magnetic field: $B_x^{(1)} = k_y E_z^{(1)}/\omega$ and $B_z^{(1)} = -k_y E_x^{(1)}/\omega$.

https://doi.org/10.1017/S0022377816001264 Published online by Cambridge University Press

The evolution of $u^{(1)}_{y,\alpha}$ completely determines that of $\Pi^{(1)}_{xx,\alpha}$ and $\Pi^{(1)}_{zz,\alpha}$ via plasma compressibility effects, but these $\boldsymbol{\Pi_\alpha}$ components are not linearly involved in the fluid velocity dynamics. In particular, equations (3.6)–(3.7) correspond to polytropic-type equations with indices '1' (3.6) and '3' (3.7) respectively. We emphasise however that, while polytropic closures with the same indices would give an equivalent description of the TSI, whose linear dispersion relation does not depend indeed on the pressure anisotropy (cf. § 4.1), the evolution of the out-of-diagonal components Π_{xy} and Π_{yz} of the pressure tensor is essential (cf. (3.3), (3.5)) to the fluid description of the TRWI, as already evidenced in the non-resonant limit of the non-relativistic WI (Sarrat *et al.* 2016). Notice that the $\Pi_{xz,\alpha}$ component remains zero during the whole linear evolution and that the two other non-diagonal components can evolve even if the equilibrium pressure is isotropic due to the first term on the right-hand side in equations (3.9) and (3.10). The role of an initial pressure anisotropy on the magnetic field generation clearly appears in the second term on the right-hand side of the two latter equations.

3.2. *Dispersion relations*

Combining linearised Maxwell and fluid equations leads to the generalised dispersion relation, $[\boldsymbol{D}]\cdot\boldsymbol{E}^{(1)}=0$, with $[\boldsymbol{D}]$ the dispersion matrix,

$$\boldsymbol{D}=\begin{bmatrix} D_{xx} & 0 & 0 \\ 0 & D_{yy} & 0 \\ 0 & 0 & D_{zz} \end{bmatrix}, \tag{3.11}$$

whose elements D_{ij} are given by

$$D_{xx}=\frac{\omega^2}{c^2}-k_y^2-\sum_\alpha \frac{\omega^2_{pe,\alpha}}{c^2}\frac{w_\alpha^2+k_y^2(c^2_{x,\alpha}-c^2_{y,\alpha})}{w_\alpha^2-k_y^2c^2_{y,\alpha}}, \tag{3.12}$$

$$D_{yy}=\frac{\omega^2}{c^2}-\frac{\omega^2}{c^2}\sum_\alpha \frac{\omega^2_{pe,\alpha}}{w_\alpha^2-3k_y^2c^2_{y,\alpha}}, \tag{3.13}$$

and

$$D_{zz}=\frac{\omega^2}{c^2}-k_y^2-\sum_\alpha \frac{\omega^2_{pe,\alpha}}{c^2}\frac{w_\alpha^2+k_y^2(c^2_{z,\alpha}-c^2_{y,\alpha})}{w_\alpha^2-k_y^2c^2_{y,\alpha}}. \tag{3.14}$$

As in the kinetic framework (Lazar *et al.* 2009), we obtain three decoupled dispersion relations in the linear regime, given by $\mathrm{Det}[\boldsymbol{D}]=0$. The relation $D_{yy}=0$ corresponds to plasma oscillations modified by the existence of the beams and damped by thermal effects: this is the fluid TSI dispersion relation. Notice that D_{yy} does not depend on the pressure anisotropy, but only on the thermal spread along the beams direction, as in the kinetic framework. The dispersion relations given by $D_{xx}=0$ and $D_{zz}=0$ are identical after replacing $c^2_{x,\alpha}$ by $c^2_{z,\alpha}$ and *vice versa*. The dispersion relation $D_{xx}=0$ depends on the pressure anisotropy and describes the time-resonant Weibel-type modes we focus on in the following.

In order to discuss the transition between the non-propagating and the time-resonant character of the Weibel dispersion relation, we make the further simplifying assumption to consider the special case of two symmetrical beams. We then write

https://doi.org/10.1017/S0022377816001264 Published online by Cambridge University Press

$n_1^{(0)} = n_2^{(0)} = n^{(0)}/2$, $u_{y,2}^{(0)} = -u_{y,1}^{(0)} = -u_0$, $c_{z,\alpha} = c_z$, $c_{y,\alpha} = c_y$, $c_{x,\alpha} = c_x \, \forall \alpha$ and $c_y \neq c_x \neq c_z$. The (3.12) and (3.13) respectively become

$$\frac{\omega^2}{c^2} - k_y^2 - \frac{\omega_{pe}^2}{2c^2} \sum_\alpha \frac{1 + \dfrac{k_y^2 (c_x^2 - c_y^2)}{w_\alpha^2}}{1 - \dfrac{k_y^2 c_y^2}{w_\alpha^2}} = 0 \tag{3.15}$$

and

$$1 - \frac{\omega_{pe}^2}{2} \sum_\alpha \frac{1}{w_\alpha^2} \frac{1}{1 - \dfrac{3k_y^2 c_y^2}{w_\alpha^2}} = 0. \tag{3.16}$$

We finally note that, should we have considered an anisotropic pressure configuration with none of the principal axes aligned with the beam and wave vector direction, i.e. with non-null out-of-diagonal equilibrium components of $\Pi_{ij,\alpha}^{(0)}$, the dispersion matrix $[\boldsymbol{D}]$ would not have been diagonal, thus implying a linear coupling between electrostatic and electromagnetic features which in the case we study here are instead well separated and related to the TSI and TRWI only.

4. The hydrodynamic limit

We introduce the parameter

$$\epsilon_\alpha \equiv \frac{k_y c_{y,\alpha}}{w_\alpha}, \tag{4.1}$$

which satisfies the criterion

$$|\epsilon_\alpha| \ll 1 \tag{4.2}$$

at the hydrodynamic limit. In the case of perpendicular propagation of WI–CFI coupled modes, it becomes the condition $k_y c_{y,\alpha}/|\omega| \ll 1$. Once satisfied for each beam, this latter criterion has been shown to grant an identical description of the linear WI–CFI modes in the kinetic and in the extended fluid models (Sarrat *et al.* 2016).

Here we show that, in this limit, the kinetic TSI and the TRWI dispersion relations are correctly described by the extended fluid model.

For the sake of simplicity and in order to allow an analytical treatment of the transition between non-time-resonant and time-resonant Weibel modes discussed in § 5, we restrict the analysis to the case of symmetric beams (3.15)–(3.16). In this case, the hydrodynamic criterion reads

$$\epsilon_\pm \equiv \frac{k_y c_y}{\sqrt{(\omega_r \mp k_y u_0)^2 + \gamma^2}} \ll 1. \tag{4.3}$$

The equivalence between the kinetic and extended fluid linear analysis in the hydrodynamic limit, discussed in §§ 4.1 and 4.2 below, can be shown to hold also for non-symmetrical beams. In this latter case, it is usually more difficult to fulfil the hydrodynamic criterion simultaneously for the two beams, especially if the temperature asymmetry between the beams is strong.

https://doi.org/10.1017/S0022377816001264 Published online by Cambridge University Press

4.1. *Two-stream instability*

For the symmetrical TSI, the kinetic dispersion relation $D_{yy} = 0$ is (Lazar *et al.* 2009)

$$0 = 1 + \frac{\omega_{pe}^2}{2}\left(\frac{1+\xi_+ Z_+}{k_y^2 c_y^2} + \frac{1+\xi_- Z_-}{k_y^2 c_y^2}\right), \tag{4.4}$$

where $Z_\pm = Z(\xi_\pm)$ is the plasma dispersion function (Fried & Conte 1961), with $\xi_+ \equiv w_+/(\sqrt{2}k_y c_y) = (\omega - k_y u_0)/(\sqrt{2}k_y c_y)$ and $\xi_- \equiv w_-/(\sqrt{2}k_y c_y) = (\omega + k_y u_0)/(\sqrt{2}k_y c_y)$.

As the symmetrical TSI is a non-propagating instability ($\omega_r = 0$ case in (4.3)), $\epsilon_+ = \epsilon_-$ and so the hydrodynamic criterion is fulfilled by the two beams. Making the assumption that $\xi_\pm \gg 1$, it becomes possible to develop the plasma dispersion function

$$Z(\xi) \sim -\frac{1}{\xi}\left(1 + \frac{1}{2\xi^2} + \frac{3}{4\xi^4}\right), \tag{4.5}$$

and, substituting (4.5) in (4.4), we find

$$0 \sim 1 - \frac{\omega_{pe}^2}{2}\left[\frac{1}{w_+^2}\left(1 + \frac{3k_y^2 c_y^2}{w_+^2}\right) + \frac{1}{w_-^2}\left(1 + \frac{3k_y^2 c_y^2}{w_-^2}\right)\right]. \tag{4.6}$$

Such a development is justified because of the behaviour of the TSI: the parallel thermal spread decreases the growth rate of this instability. One has to retain the term of order four in ξ in the development of Z to preserve some thermal effects in the dispersion relation. The final contribution of this term is only of order ξ^{-2}.

If we perform a Taylor expansion of the fluid dispersion relation (3.16) for $\epsilon_\alpha \ll 1$, we recover (4.6) implying the equivalence of the fluid and the kinetic descriptions when $\epsilon_\alpha \ll 1$ simultaneously for the two beams.

4.2. *Weibel-like modes*

The kinetic dispersion relation $D_{xx} = 0$ (or $D_{zz} = 0$) for the symmetrical Weibel-like modes is (Lazar *et al.* 2009)

$$\frac{k_y^2 c^2}{\omega^2} = 1 + \frac{\omega_{pe}^2}{\omega^2}\left(A + \frac{A}{2}(\xi_+ Z_+ + \xi_- Z_-) - 1\right), \tag{4.7}$$

where we define the anisotropy parameter $A \equiv c_x^2/c_y^2$.

Again we assume $\xi_\pm \gg 1$ and obtain the hydrodynamic dispersion relation

$$\frac{k_y^2 c^2}{\omega^2} \simeq 1 - \frac{\omega_{pe}^2}{\omega^2}\left[1 + \frac{A}{2}\left(\frac{k_y^2 c_y^2}{w_+^2} + \frac{k_y^2 c_y^2}{w_-^2}\right)\right]. \tag{4.8}$$

We have neglected all the terms greater than $\epsilon_\pm^2$. This dispersion relation coincides with the corresponding limit taken for the fluid dispersion relation (3.15).

5. Time-resonant Weibel instability

From now on we focus on the dispersion relation of Weibel-like modes, $D_{xx} = 0$. The numerical analysis of the kinetic dispersion relation performed by Lazar *et al.* (2010) already evidenced the existence of a critical wavenumber k_{SB}, at which a 'slope

https://doi.org/10.1017/S0022377816001264 Published online by Cambridge University Press

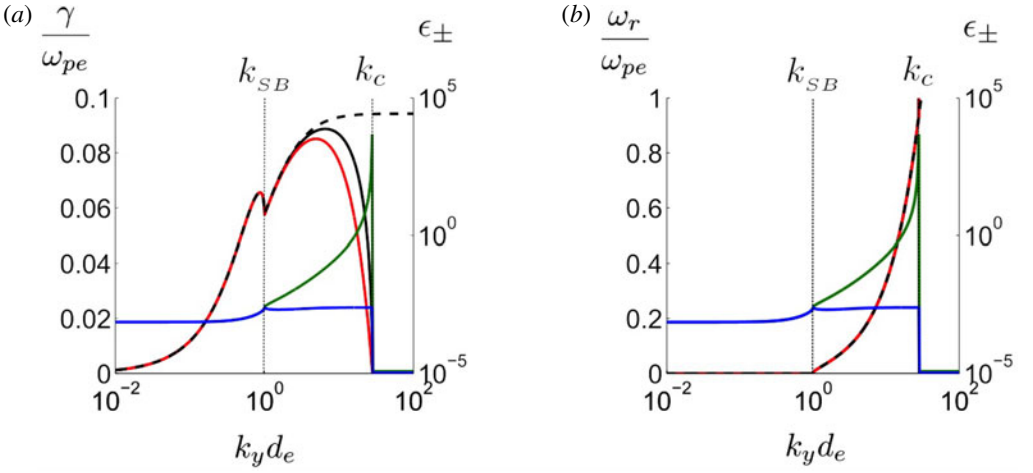


FIGURE 2. Comparison between kinetic (red line) and fluid (black line) growth rates (*a*) and corresponding frequencies (*b*) of the most unstable modes. The black dotted line corresponds to the values of ω_r and γ obtained with (4.8), i.e. by applying the hydrodynamic limit. Differences between fluid and kinetic models are more important for the growth rate than for the frequency of the more unstable solution. In (*b*), the three curves overlap. Blue and green lines correspond to the value of $\epsilon_\pm$, computed with the kinetic value of ω for the two beams (the green curve being for ϵ_-, cf. (4.3)). Physical parameters: $u_0 = 1/30$, $c_x = u_0 + 0.1$ and $c_y = u_0/10$.

breaking' of the growth rate occurs (cf. figure 2), and the non-propagating nature of the most unstable mode that exists for $k_y < k_{SB}$. Here we show that the extended fluid approach allows an accurate description of such a transition and, moreover, makes it possible to identify the features of six roots of the dispersion relation and in particular of the second non-propagating mode met for $k_y < k_{SB}$: the slope breaking is then found to correspond to a bifurcation point, at which the two couples of non-propagating unstable modes existing for $k_y < k_{SB}$ merge into the four time-resonant growing and decaying modes found for $k_y > k_{SB}$. The two growing modes – and also the two decaying ones – propagate in opposite directions (figure 3).

A second bifurcation point is found at the critical wavenumber $k_y = k_c$ at which the growth rate of the unstable modes becomes zero (figure 3): for $k_y > k_c$, all modes have now become purely propagating. Two former unstable modes propagate in each direction, with different values of ω_r.

In order to show this, let us first discuss the accuracy of the fluid description in reproducing the known kinetic results (§ 5.1). Then we will focus on the resolution of the fluid dispersion relation, which allows an analytic solution from which these results can be deduced (§ 5.2). Then, in § 5.3 we comment on the validity of these results in the kinetic regime.

5.1. *Transition to the time-resonant WI in the fluid and kinetic description*

Figure 2(*a*) displays a comparison between the maximal growth rates obtained by integrating the fluid model, the kinetic model (both with no approximation) and the hydrodynamic limit of the two. The corresponding real frequencies, numerically obtained from (3.15) and (4.7), are sketched in figure 2(*b*). We used for this a set of

https://doi.org/10.1017/S0022377816001264 Published online by Cambridge University Press

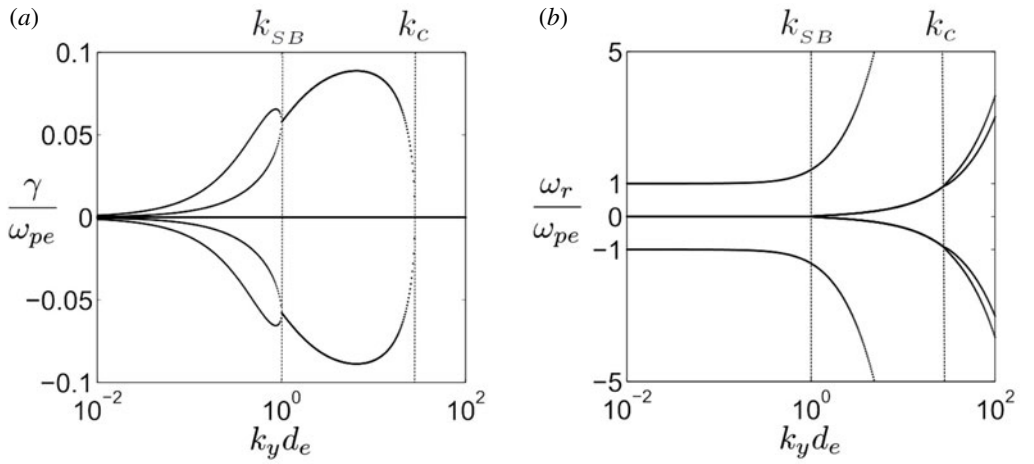


FIGURE 3. Roots of (5.1): growth rates (a), frequencies (b). The two panels display, for any value of k_y, the behaviour of a total of six modes. The slope breaking observed in figure 2 for the growth rate corresponds to a merging of two unstable modes. Two other modes (characterised by $\omega_r \geqslant \omega_{pe}$) are stable for any value of k_y. Physical parameters: $u_0 = 1/30$, $c_x = u_0 + 0.1$ and $c_y = u_0/10$.

non-relativistic parameters: $u_0 = 1/30$, $c_x = u_0 + 0.1$ and $c_y = u_0/10$. Two points shall be highlighted.

Regarding the discrepancies between the fluid and kinetic descriptions, one remarks a very good agreement between fluid and kinetic values of ω_r: differences between the two models and their hydrodynamic limit are negligible, even when $\epsilon_\pm$ is not. This is not the case of the growth rate, for which discrepancies between fluid and kinetic values increase with the wavenumber. However, they tend to coincide again at the cutoff value k_c, which is almost identical in the fluid and kinetic models, next to which the hydrodynamic limit fails (the cutoff wavenumber disappears, instead, in the hydrodynamic limit (4.8)). The same kind of behaviour was remarked for the pure WI and for the WI–CFI coupled modes (Sarrat *et al.* 2016).

Concerning instead the dependence of ω_r and γ on the wavenumber k_y, for the set of parameters of figure 2(b) one remarks the increase of ω_r between $k_{SB}d_e \sim 1$ and $k_c d_e \sim 30$. As evidenced by Lazar *et al.* (2010), this behaviour is characteristic of the time-resonant WI, whose transition at $k_{SB}d_e \sim 1$ occurs in figure 2 in the 'hydrodynamic' regime (both beams have $|\epsilon_\pm| \ll 1$ around $k_y = k_{SB}$). The curves of the three growth rates exhibit the same slope breaking at k_{SB}, indicating that for these parameters the pressure tensor based model gives an accurate description of the transition.

Therefore, besides being accurate for values of k_y smaller than k_c, yet comparable to or larger than k_{SB}, the results of the linear analysis in the extended fluid model are reliable also outside the hydrodynamic limit, although with some quantitative differences with respect to the kinetic result. To study the behaviour of the modes given by the roots of (4.7), we then rely on the fluid dispersion relation (3.15), which has the advantage of allowing a simpler analytical treatment due to its polynomial form in ω and in k_y.

https://doi.org/10.1017/S0022377816001264 Published online by Cambridge University Press

5.2. *Discussion of the fluid dispersion relation*

The fluid dispersion relation (3.15) gives a polynomial of degree three in ω^2,

$$\begin{aligned} 0 \;=\; & \omega^6 - \omega^4[\omega_{pe}^2 + k_y^2c^2 + 2k_y^2(u_0^2 + c_y^2)] \\ & + \omega^2[k_y^4(u_0^2 - c_y^2)^2 + 2k_y^2(u_0^2 + c_y^2)(\omega_{pe}^2 + k_y^2c^2) - \omega_{pe}^2k_y^2c_x^2] \\ & - k_y^4(c_y^2 - u_0^2)[k_y^2c^2(c_y^2 - u_0^2) - \omega_{pe}^2(u_0^2 + c_x^2 - c_y^2)]. \end{aligned} \tag{5.1}$$

which implies the existence of three couples of complex roots. These roots are evidenced in figure 3, where a numerical solution of (5.1) is provided for the same parameters of figure 2.

Although it is in principle possible to write the explicit general form of the roots of (5.1), for the purpose to identify the propagating or unstable behaviour of the modes in the intervals $k_y \leqslant k_{SB}$, $k_{SB} \leqslant k_y \leqslant k_c$ and $k_y > k_c$, it is sufficient to discuss the existence of the real and imaginary parts of the ω^2 solutions. Rewriting (5.1) in a more compact form,

$$W^3 + a_2W^2 + a_1W + a_0 = 0, \tag{5.2}$$

with $W \equiv \omega^2$, we look at the sign of (Abramovitz 1965)

$$\Delta \equiv q^3 + r^2, \tag{5.3}$$

where

$$q = \tfrac{1}{3}a_1 - \tfrac{1}{9}a_2^2, \quad r = \tfrac{1}{6}(a_1a_2 - 3a_0) - \tfrac{1}{27}a_2^3. \tag{5.4a,b}$$

When $\Delta > 0$, one root is real and two are complex conjugate. In the opposite case $\Delta < 0$, the irreducible case, there are three different real solutions, while if $\Delta = 0$, all the roots are real and at least two of them coincide.

The most general expressions for the three solutions in ω^2 read

$$\omega_0^2 = \underbrace{[r + \Delta^{1/2}]^{1/3}}_{s_+} + \underbrace{[r - \Delta^{1/2}]^{1/3}}_{s_-} - \frac{a_2}{3} \tag{5.5}$$

and

$$\omega_\pm^2 = -\frac{1}{2}(s_+ + s_-) - \frac{a_2}{3} \pm \frac{\mathrm{i}\sqrt{3}}{2}(s_+ - s_-). \tag{5.6}$$

As $W = \omega^2 = \omega_r^2 - \gamma^2 + \mathrm{i}2\omega_r\gamma$, the only possibility of obtaining a real ω^2 is $\omega_r = 0$ or $\gamma = 0$, that is, to have purely propagating or purely unstable modes, whereas an unstable propagating mode corresponds to a complex value of ω^2. This allows us to characterise, in terms of the sign of Δ, the three regions in the k_y parameter space identified above and evidenced in the example of figure 3. Moreover, as the discriminant Δ is a continuous function of k_y, the slope breaking k_{SB} and the cutoff wavenumber k_c correspond to the roots of the equation $\Delta(k_y) = 0$. This gives a criterion to determine *a priori* whether the WI is time resonant or strictly growing – or damped. Let us discuss under this light the three regions of figure 3.

$k_y < k_{SB}$ *region*: here the discriminant Δ is negative, ensuring three strictly different real values for ω^2, either purely propagating of purely unstable. The two stable modes propagating in opposite directions and characterised by $|\omega_r| \geqslant \omega_{pe}$ correspond to linearly polarised electromagnetic waves. The four other modes consist of two non-propagating and growing Weibel-type modes and of their two damped

https://doi.org/10.1017/S0022377816001264 Published online by Cambridge University Press

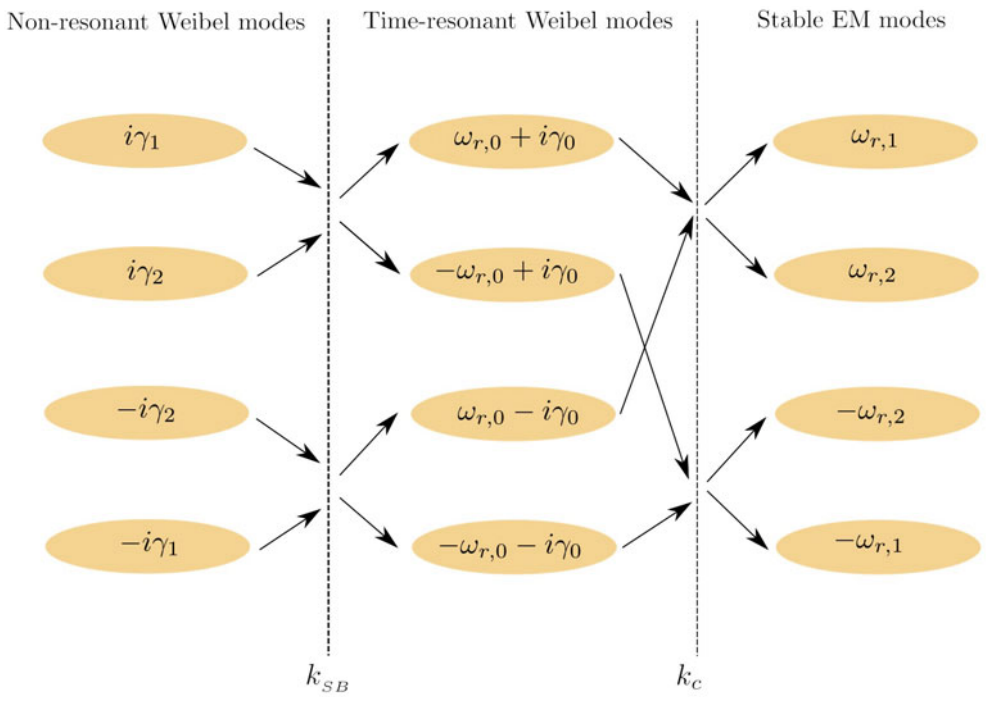


FIGURE 4. Complex general expression of the four unstable modes as a function of the wavenumber. Black arrows indicate a merging or a breaking of degeneracy of two modes at a bifurcation. The bifurcations, at $k_y = k_{SB}$ and $k_y = k_c$, are indicated by the dashed vertical lines. Here, subscripts $\alpha = 1, 2$ generically label different values for γ and ω_r.

counterparts, which evolve on long time scales with respect to the inverse electron oscillation time, $\gamma \ll \omega_{pe}$. For the set of parameters of figure 3, a local maximum in the growth rates can be identified around $k_y d_e \sim 0.8$.

$k_y = k_{SB} \sim d_e^{-1}$ represents a 'double' bifurcation point in the (k_y, ω) space, which solves $\Delta(k_y) = 0$. At the slope breaking of γ, first observed by Lazar *et al.* (2010), the two purely growing (damped) roots, distinct for $k_y < k_{SB}$, acquire the same growth rate and a propagating character, pairwise, in opposite directions.

$k_{SB} < k_y < k_c$ *region*: here, where time-resonant unstable modes are encountered, $\Delta > 0$. The time-resonant Weibel modes, propagating in opposite directions (same γ and opposite ω_r), are described by the roots ω_+^2 and ω_-^2 (5.6). Moreover, the damped and growing modes are complex conjugates. The stable electromagnetic waves already encountered for $k_y < k_{SB}$ are given by the only real root $W = \omega_0^2$ (5.5).

$k_y = k_c$ is the point at which the unstable part of the solutions vanish. It corresponds again to a 'double' bifurcation in the (k_y, ω) space, once more given by $\Delta(k_c) = 0$.

In the $k_y > k_c$ region, where $\Delta < 0$ again, all modes maintain their propagating character with two different couples of values of ω_r, pairwise opposite in sign. All modes propagating above this critical wavenumber are stable, linearly polarised electromagnetic waves.

The nature of the six fluid modes in these three regions of the wavenumber space is summarised in figure 4.

https://doi.org/10.1017/S0022377816001264 Published online by Cambridge University Press

5.2.1. *Low-frequency approximation*

Further insight on the behaviour of the unstable modes comes from the restriction to low frequencies $|\omega| \ll \omega_{pe}$, which implies the exclusion of the stable solutions and thus the reduction of (5.1) to a polynomial of degree two in ω^2:

$$\begin{aligned} 0 \;=\; & \omega^4[\omega_{pe}^2 + k_y^2c^2] - \omega^2[2k_y^2(u_0^2 + c_y^2)(\omega_{pe}^2 + k_y^2c^2) - \omega_{pe}^2k_y^2c_x^2] \\ & + k_y^4(c_y^2 - u_0^2)[k_y^2c^2(c_y^2 - u_0^2) - \omega_{pe}^2(u_0^2 + c_x^2 - c_y^2)]. \end{aligned} \tag{5.7}$$

It turns out that the growth rate and the real frequency of the four modes remain practically unchanged under this approximation. For example, for the parameters used in figure 2, the maximal growth rate in the non-resonant and in the time-resonant regime undergo a variation of $\sim$0.1 %, whereas k_c and k_{SB} vary less than 0.1 %.

With similar arguments to those previously developed to analyse the roots of (5.1), we obtain quite accurate analytical estimations of the slope-breaking and cutoff wavenumbers. We thus look for the roots of $\Delta_*(k_y) = 0$, where Δ_* is the discriminant of (5.7), which reads

$$\Delta_* = k_y^4\{[16u_0^2c_y^2c^4]k_y^4 + 8\omega_{pe}^2u_0^2c^2[4c_y^2 - c_x^2]k_y^2 + \omega_{pe}^4[c_x^4 + 8u_0^2(2c_y^2 - c_x^2)]\}. \tag{5.8}$$

The roots of the above polynomial correspond to real values of k_y^2 when $c_y^2 < u_0^2$ (condition met for the set of parameters of figure 3). Under this hypothesis, the slope-breaking and the cutoff wavenumbers respectively read:

$$k_{SB}^2d_e^2 = \frac{1}{4}\left[\frac{c_x^2}{c_y^2}\left(1 - \sqrt{1 - \frac{c_y^2}{u_0^2}}\right) - 4\right], \quad k_c^2d_e^2 = \frac{1}{4}\left[\frac{c_x^2}{c_y^2}\left(1 + \sqrt{1 - \frac{c_y^2}{u_0^2}}\right) - 4\right]. \tag{5.9a,b}$$

For the parameters of figure 3, for example, the values $k_{SB} = 1.0025$ and $k_c = 28.2311$ are obtained, in good agreement with the numerical solution of (5.1).

The analytical estimation of k_{SB} given by Lazar *et al.* (2010) in the hydrodynamic regime is recovered by taking the further limit $c_y \ll u_0$, for which (5.9) becomes:

$$k_{SB}d_e \simeq \sqrt{\frac{c_x^2}{8u_0^2} - 1}; \quad k_cd_e \simeq \frac{c_x}{\sqrt{2}c_y}. \tag{5.10a,b}$$

The limit case $u_0 = c_y$ is particularly interesting as it implies the absence of the time-resonant solutions due to the superposition of the roots

$$k_{SB}d_e = k_cd_e = \sqrt{\frac{c_x^2}{4c_y^2} - 1}. \tag{5.11}$$

Only the non-propagating Weibel modes remain. One remarks the strong similarity between (5.11) and the cutoff wavenumber of the pure WI modes, $k_c^{WI} = \sqrt{c_x^2/c_y^2 - 1}$, as for $c_y = u_0$ the sixth-order polynomial dispersion relation (5.1) becomes

$$0 = \omega^4 - \omega^2[\omega_{pe}^2 + k_y^2(c^2 + 4c_y^2)] + k_y^2[k_y^2c^24c_y^2 - \omega_{pe}^2(c_x^2 - 4c_y^2)]. \tag{5.12}$$

This represents, indeed, the pure WI dispersion relation as obtained in the fluid framework (cf. (22) of Sarrat *et al.* 2016), with an effective squared 'thermal' velocity

https://doi.org/10.1017/S0022377816001264 Published online by Cambridge University Press

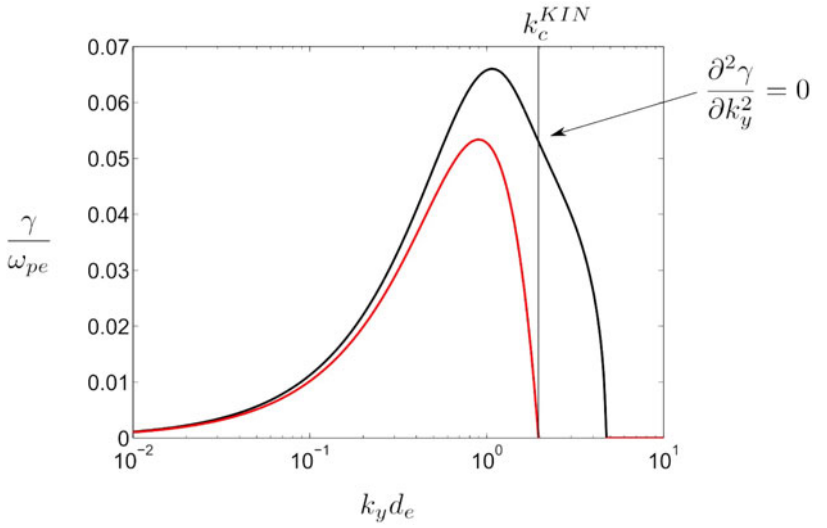


FIGURE 5. Comparison between fluid (black) and kinetic (red) growth rates for $u_0 = 1/30$, $c_y = u_0 + 0.01$ and $c_x = u_0 + 0.1$. The spurious inflection point on the fluid growth rate is observed when k_y is close to the kinetic cutoff k_c^{KIN}.

defined as $\tilde{c}_y^2 = 4c_y^2$. This specific point can be understood considering each beam as represented by a bi-Maxwellian distribution function, whose standard deviations in the velocity space are $\sigma_i = c_i$, with $i = x, y$: when $c_y = u_0$, the two Maxwellian are so close that they shape one single Maxwellian with standard deviation $\widetilde{\sigma}_i = 2\sigma_i$.

If $c_y > u_0$ the two distribution functions overlap and a part of the information contained in each of them is lost. We can then expect that these non-resonant Weibel modes will persist in the fluid description until $\widetilde{c}_y$ becomes comparable to c_x. A comparison between fluid and kinetic solutions (figure 5) shows that both descriptions lead to a non-resonant instability. However, the fluid growth rate exhibits an inflection point around the kinetic cutoff which does not exist in the kinetic description: once more, this suggests that close to the kinetic cutoff wavenumber, the inclusion of higher-order velocity moments in the fluid model becomes necessary.

5.2.2. *Low-frequency, small-wavenumber limit*

A simplified analytical expression for the growth rates of the non-resonant Weibel modes existing for $k_y < k_{sB}$ can be obtained by further considering the $k_y d_e \ll 1$ limit of (5.7):

$$\omega^4 - \omega^2[2k_y^2(u_0^2 + c_y^2) - k_y^2 c_x^2] + k_y^4(c_y^2 - u_0^2)(c_y^2 - u_0^2 - c_x^2) = 0. \tag{5.13}$$

Its discriminant reads:

$$\Delta_{**} = k_y^4 c_x^4 \left[1 + \frac{8u_0^2}{c_x^2}\left(\frac{2c_y^2}{c_x^2} - 1\right)\right] = k_y^4[c_x^4 + 8u_0^2(2c_y^2 - c_x^2)] \tag{5.14}$$

and its sign does not depends on the value of k_y. Consequently the bifurcations disappear.

https://doi.org/10.1017/S0022377816001264 Published online by Cambridge University Press

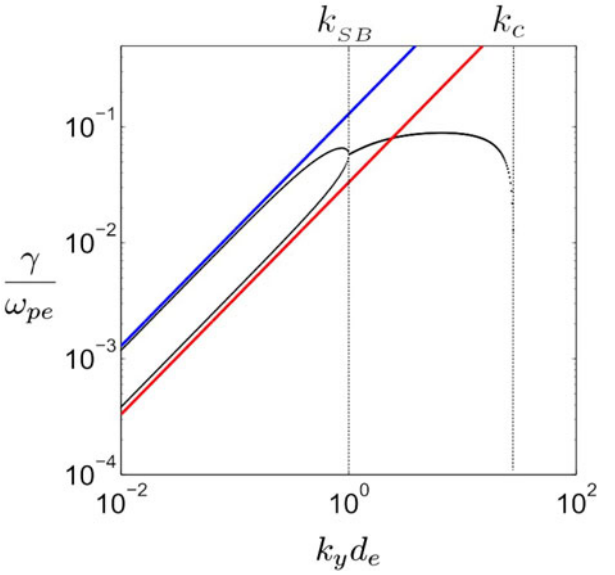


FIGURE 6. The two asymptotic solutions (blue and red lines) of the purely growing modes for $k_y d_e \ll 1$. Same parameters of figures 2 and 3.

Consider now the strong anisotropy limit expressed by $c_y \ll u_0 \ll c_x$, which is, for example, the one represented in figures 2 and 3 (with Δ_{**} scaling as $10^{-4}k_y^4$). This corresponds to the case $\Delta_{**} > 0$. This assumption leads us to the following asymptotic estimates for the two solutions in ω^2 and for the corresponding growth and damping rates (figure 6),

$$\omega^2 \simeq -k_y^2(u_0^2 - c_y^2), \quad \gamma \simeq \pm k_y u_0 \sqrt{1 - \frac{c_y^2}{u_0^2}} \quad \text{(least unstable mode)}, \tag{5.15a,b}$$

$$\omega^2 \simeq -k_y^2(c_x^2 - 3u_0^2), \quad \gamma \simeq \pm k_y c_x \sqrt{1 - \frac{3u_0^2}{c_x^2}} \quad \text{(most unstable mode)}, \tag{5.16a,b}$$

which, as expected, are non-propagating.

Two time-resonant unstable modes can be obtained instead for $\Delta_{**} < 0$. Since the discriminant of $\Delta_{**}(c_x^2) = 0$ is $64u_0^2(u_0^2 - c_y^2)$, we deduce that in this case $\Delta_{**} < 0$ if $c_{x-}^2 < c_x^2 < c_{x+}^2$, with

$$c_{x,\pm}^2 = 4u_0^2 \left(1 \pm \sqrt{1 - \frac{c_y^2}{u_0^2}}\right). \tag{5.17}$$

Assuming in particular, with no loss of generality, $c_y \ll u_0$ then $c_{x,+} \simeq \sqrt{2(4u_0^2 - c_y^2)}$ $\simeq 2\sqrt{2}u_0$ and $c_{x,-} \simeq \sqrt{2}c_y$. This result agrees with (5.10) for the slope breaking: for $c_y \ll u_0$, when $c_x < 2\sqrt{2}u_0$ the Weibel instability is always propagating.

To illustrate this point, let us consider a numerical example for parameters fitting in the upper bound of the interval $\Delta_{**} < 0$: choosing $u_0 = 1/30$, $c_y = u_0/10$, which fulfil the conditions $c_y \ll u_0$ and $c_x = \sqrt{2}u_0 \lesssim c_{x,+}$, then $\Delta_{**} \simeq -1,\ 5 \times 10^{-5}k_y^4$. The

https://doi.org/10.1017/S0022377816001264 Published online by Cambridge University Press

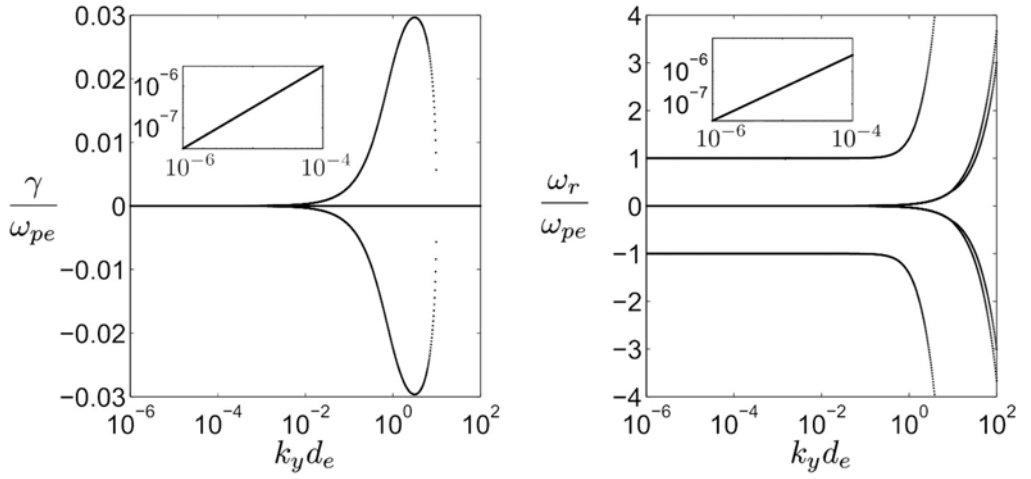


FIGURE 7. Numerical solution of the fluid dispersion relation (5.1) for $u_0 = 1/30$, $c_y = u_0/10$ and $c_x = \sqrt{2}u_0$ (then $\Delta_{**} \simeq -1,\ 5 \times 10^{-5} k_y^4$).

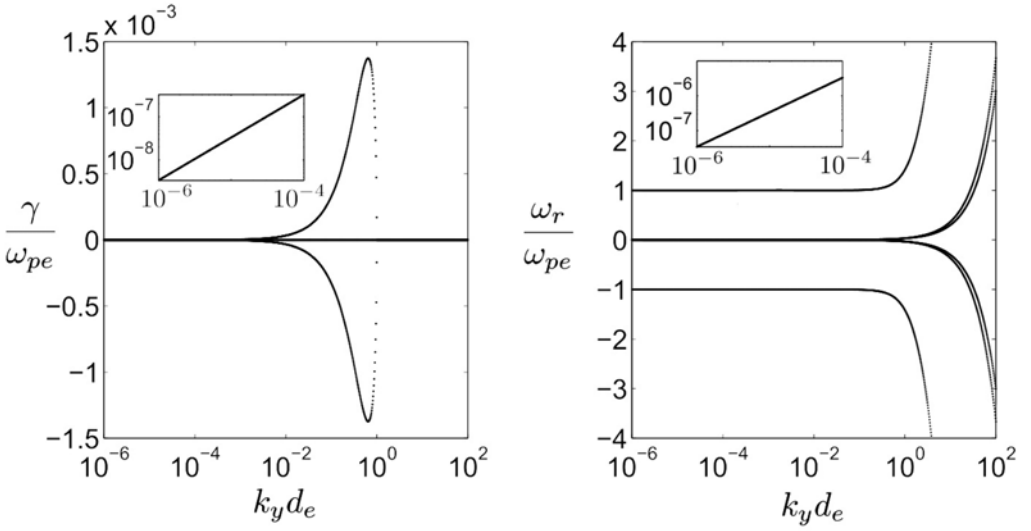


FIGURE 8. Numerical solution of the fluid dispersion relation (5.1) for $u_0 = 1/30$, $c_y = u_0/10$ and $c_x = 2c_y$ (then $\Delta_{**} \simeq -2 \times 10^{-7} k_y^4$).

solutions of the exact fluid dispersion relation (5.1) are displayed in figure 7. Note that, because of this, the assumptions $k_y d_e \ll 1$ and $|\omega| \ll \omega_{pe}$ do not intervene in this result. Looking at the sign of the discriminant Δ of the exact fluid dispersion relation (5.1), the represented curve is recognised to correspond to the TRWI, with a value of k_c which is well approximated by the corresponding estimation of (5.10): Δ is positive for $k_y < k_c \sim 10 d_e^{-1}$, zero at $k_y = k_c$ and negative for $k_y > k_c$.

Let us focus now on the lower bound of the $\Delta_{**} < 0$ interval, by choosing $u_0 = 1/30$, $c_y = u_0/10$ and $c_x = 2c_y$, so that $\Delta_{**} \simeq -2 \times 10^{-7} k_y^4$. Results are shown in figure 8. As

https://doi.org/10.1017/S0022377816001264 Published online by Cambridge University Press

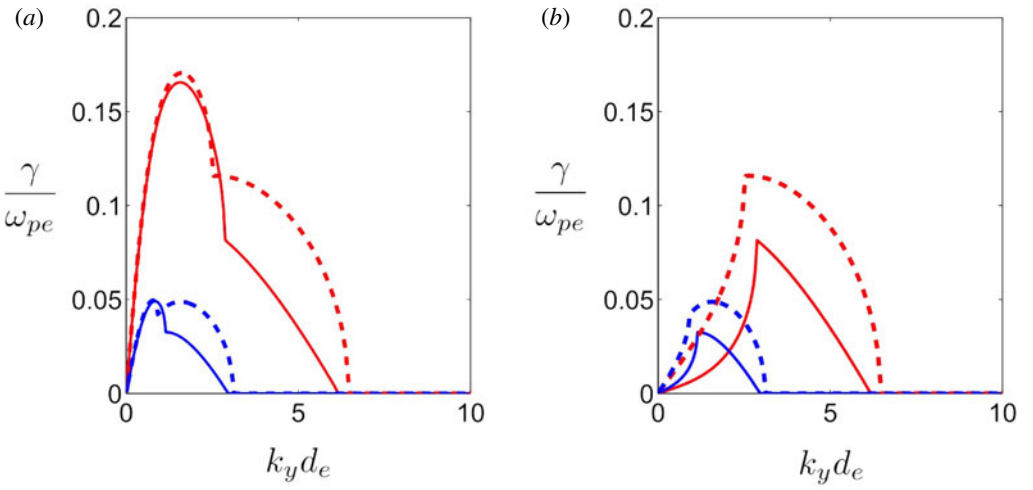


FIGURE 9. Comparison between fluid (dashed lines) and kinetic (solid lines) growth rates corresponding to the upper (*a*) and to the lower (*b*) unstable branches of the Weibel instability. Blue curves are obtained for $u_0 = 1/30$, $c_y = u_0/\sqrt{2}$ and $c_x = 10c_y$. Red curves are obtained for $u_0 = 1/30$, $c_y = u_0/\sqrt{2}$ and $c_x = 5c_y$. A direct comparison with figure 1 in Lazar *et al.* (2010) can be made.

expected, due to the smaller thermal anisotropy, the growth rate is smaller than the one considered in figure 7, but the qualitative behaviour is the same.

Finally, $\Delta_{**} > 0$ and there are no more unstable modes when $c_x \lesssim c_{x,-}$ because the transverse thermal energy is not sufficient anymore to drive the Weibel-type mode.

5.3. *Full kinetic description*

Although with some quantitative differences in the numerical estimations of the growth rates and critical wavenumbers, the existence and characterisation of the sixth roots of the fluid dispersion relation (5.1) in the three intervals of the wavenumber space, $k_y < k_{SB}$, $k_{SB} < k_y < k_c$ and $k_c < k_y$, are confirmed in a full kinetic description, even when the hydrodynamic limit is not satisfied. In particular, the second unstable mode evidenced in figure 3 can be generally identified also in the kinetic framework (we note in passing the usefulness of the fluid solution as an initial seed for the numerical kinetic solver).

An example of this solution is shown in figure 9, where the growth rate of the lower non-resonant Weibel unstable branch is represented as a function of the wavenumber, for parameters which do not satisfy the hydrodynamic criterion. The fluid model overestimates the kinetic growth rate, but k_{SB} is approximately the same. Note that due to the lower value of $|\omega|$, the hydrodynamic criterion is harder to achieve for the lower branch than for the upper branch.

The role of thermal effects on the transition to the TRWI, characterised in terms of the fluid analysis in § 5.2.2, is also recovered in the kinetic framework. As an example, in figures 10 and 11 we show a comparison of the fluid and kinetic growth rates and real frequencies for the most unstable mode analysed in figures 7 and 8 respectively.

For the case of figure 10 the agreement is excellent, consistent with the fulfilment of the hydrodynamic criterion for this set of parameters. We can expect, also in the

https://doi.org/10.1017/S0022377816001264 Published online by Cambridge University Press

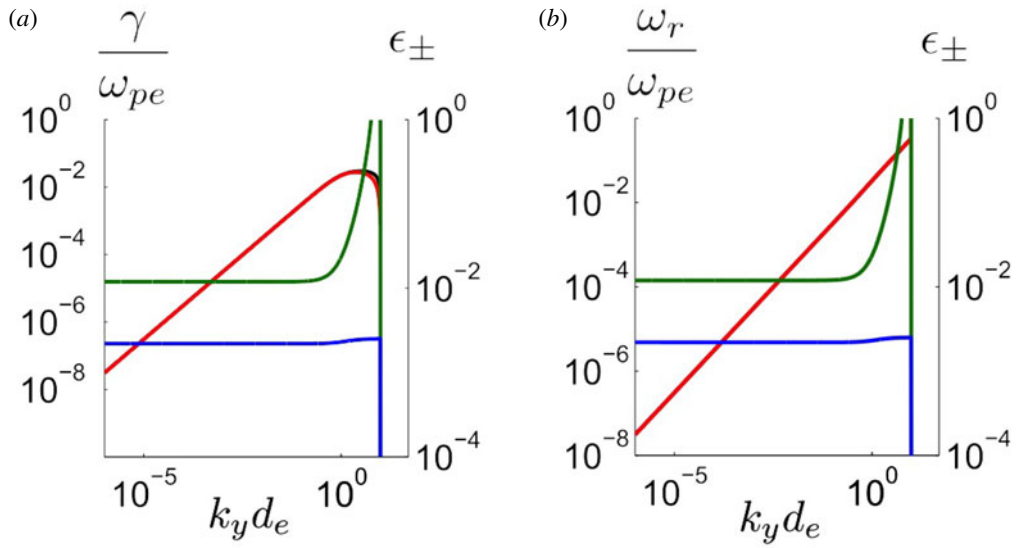


FIGURE 10. Comparison between kinetic (red line) and fluid (black line) maximal growth rates (*a*) and corresponding frequencies (*b*). Blue and green lines corresponds to the hydrodynamic criterion $\epsilon_\alpha = k_y c_y/\Omega_\alpha$ values for the two beams, computed with the kinetic value of ω. The physical parameters are the same than for figure 7: $u_0 = 1/30$, $c_x = \sqrt{2}u_0$ and $c_y = u_0/10$. Differences between the two models appear only near of the cutoff.

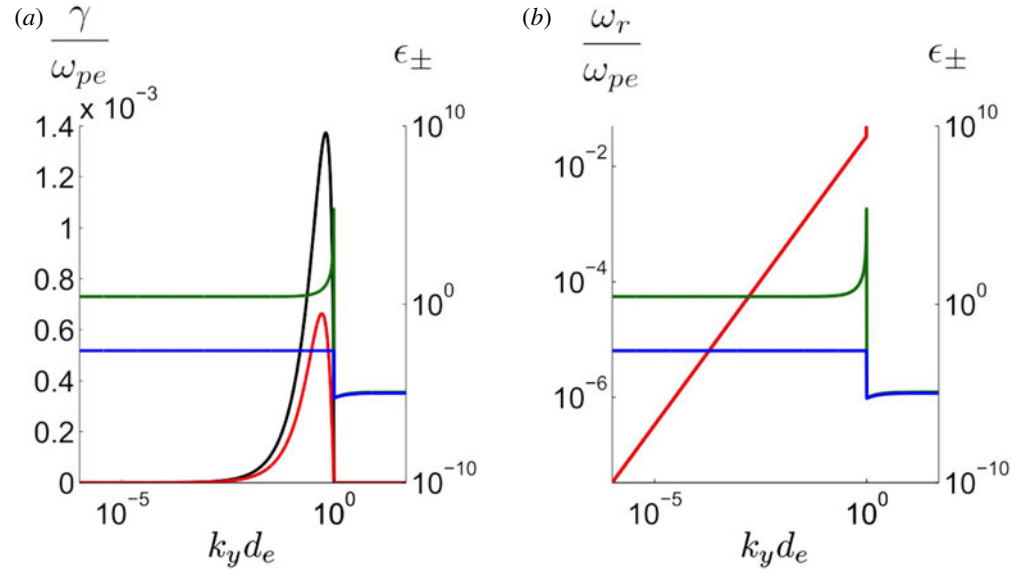


FIGURE 11. Comparison between kinetic (red line) and fluid (black line) maximal growth rates (*a*) and corresponding frequencies (*b*). Blue and green lines corresponds to the value of the hydrodynamic criterion ϵ_α for the two beams. The physical parameters are the same than for figure 8: $u_0 = 1/30$, $c_y = u_0/10$ and $c_x = 2c_y$. The hydrodynamic limit is never reached, but the two models predict a Resonant Weibel regime whatever k_y. If the differences between the growth rate values are substantial, the agreement between the two descriptions for the real frequency is very good.

https://doi.org/10.1017/S0022377816001264 Published online by Cambridge University Press

kinetic case, the disappearance of the non-resonant instability in favour of the time-resonant one, when the condition $c_{x-}^2 < c_x^2 < c_{x+}^2$ is fulfilled, as the behaviour observed for $k_y d_e \sim 10^{-6}$ is the same to that observed at arbitrarily smaller wavenumber. Indeed, the terms $\sim k_y^8$ and $\sim k_y^6$ in (5.8) are dominated by those proportional to k_y^4.

Nevertheless, the qualitative agreement is excellent also for the case of figure 11, which is largely outside the hydrodynamic regime, though quantitative differences are important here: the fluid model largely overestimates the kinetic value of the maximal growth rate. It remains however correctly smaller than the fluid one displayed on figure 10, as expected due to the relatively smaller initial anisotropy. Remarkably, the fluid and kinetic estimations of k_c and of ω_r for the TRWI appear to be in excellent quantitative agreement also in this case.

6. Conclusion

In this work we have shown that an extended fluid description which takes into account the full pressure tensor dynamics makes it possible to reproduce important features of Weibel-type instabilities excited by perturbations parallel to two counterstreaming beams, such as the existence of time-resonant (propagating) modes. By restricting ourselves to the case of symmetric beams, we have evidenced an excellent quantitative agreement between the fluid and kinetic linear description of both the TSI and the Weibel-like modes in the hydrodynamic limit (§ 4). We have then shown how the behaviour of the fluid modes agrees qualitatively and, partially, quantitatively, with the kinetic description also outside of this hydrodynamic regime (§ 5).

We have shown that this fluid description makes possible an analytical identification of various features of these Weibel-like modes in the parameter space. For example, this approach has allowed us to evidence a second purely unstable mode in the non-resonant regime, whose existence is attested also in the kinetic framework even when the hydrodynamic assumption is not satisfied. The slope breaking in the growth rate, first observed by Lazar *et al.* (2010), is then found to correspond to a bifurcation point of two unstable non-resonant modes, which completely disappears for a sufficiently small initial anisotropy (a condition which leads, instead, to a purely TRWI – § 5.2.2).

Future numerical investigations will tell whether the fluid description of these Weibel-type modes remains consistent also during their nonlinear evolution, a possibility which would imply a remarkable gain in terms of the computational cost of nonlinear simulations. In this regard we remark the interest of this analysis also as a further step towards the fluid modelling of more general two-dimensional anisotropic configurations. The 'macroscopic' insight allowed by this fluid description will hopefully help to better identify the characteristics of the so-called oblique Weibel-type instabilities occurring in this configuration, in which the features of Weibel, CFI and TSI modes are coupled.

REFERENCES

ABRAMOVITZ, M. 1965 Elementary analytical methods. In *Handbook of Mathematical Functions with Formulas, Graphs and Mathematical Tables* (ed. M. Abramovitz & I. A. Stegun), pp. 113–138. National Bureau of Standards.

ALBRECHT-MARC, M., GHIZZO, A., JOHNSTON, T. W., RÉVEILLÉ, T., DEL SARTO, D. & BERTRAND, P. 2007 Saturation processes induced by vortex-merging in numerical Vlasov–Maxwell experiments of stimulated Raman backscattering. *Phys. Plasmas* **14**, 072704.

https://doi.org/10.1017/S0022377816001264 Published online by Cambridge University Press

BASU, B. 2002 Moment equation description of Weibel instability. *Phys. Plasmas* **9**, 5131–5134.

BRET, A., FIRPO, M. C. & DEUTSCH, C. 2005 Electromagnetic instabilities for relativistic beam–plasma interaction in whole k space: nonrelativistic beam and plasma temperature effects. *Phys. Rev.* E **72** (1), 016403.

BRET, A., GREMILLET, L. & BELLIDO, J. C. 2007 How really transverse is the filamentation instability? *Phys. Plasmas* **14** (3), 032103.

BRET, A., GREMILLET, L. & DIECKMANN, M. E. 2010 Multidimensional electron beam–plasma instabilities in the relativistic regime. *Phys. Plasmas* **17** (12), 120501.

BRET, A., STOCKEM, A., NARAYAN, R. & SILVA, L. O. 2014 Collisionless Weibel shocks: full formation mechanism and timing. *Phys. Plasmas* **21** (7), 072301.

CALIFANO, F., ATTICO, N., PEGORARO, F., BERTIN, G. & BULANOV, S. V. 2001 Fast formation of magnetic islands in a plasma in the presence of counterstreaming electrons. *Phys. Rev. Lett.* **86** (23), 5293–5296.

CALIFANO, F., DEL SARTO, D. & PEGORARO, F. 2006 Three-dimensional magnetic structures generated by the development of the filamentation (Weibel) instability in the relativistic regime. *Phys. Rev. Lett.* **96** (10), 105008.

CALIFANO, F., PEGORARO, F. & BULANOV, S. V. 1997 Spatial structure and time evolution of the Weibel instability in collisionless inhomogeneous plasmas. *Phys. Rev.* E **56** (1), 963–969.

CALIFANO, F., PRANDI, R., PEGORARO, F. & BULANOV, S. V. 1998 Nonlinear filamentation instability driven by an inhomogeneous current in a collisionless plasma. *Phys. Rev.* E **58** (6), 7837–7845.

DEL SARTO, D., PEGORARO, F. & CALIFANO, F. 2016 Pressure anisotropy and small spatial scales induced by velocity shear. *Phys. Rev.* E **93** (5), 053203.

DEL SARTO, D., PEGORARO, F. & TENERANI, A. 2017 'Magneto-elastic' waves in an anisotropic magnetised plasma. *Plasma Phys. Contoll. Fusion*, to appear, http://dx.doi.org/10.1088/1361-6587/aa56bd.

DENAVIT, J. 1992 Absorption of high-intensity subpicosecond lasers on solid density targets. *Phys. Rev. Lett.* **69** (21), 3052–3055.

FRANCI, L., HELLINGER, P., MATTEINI, L., VERDINI, A. & LANDI, S. 2016 Two-dimensional hybrid simulations of kinetic plasma turbulence: current and vorticity vs proton temperature. *AIP Conf. Proc.* **1720** (1), 040003.

FRIED, B. D. 1959 Mechanism for instability of transverse plasma waves. *Phys. Fluids* **2** (3), 337.

FRIED, B. D. & CONTE, S. D. 1961 *The Plasma Dispersion Function*. Academic Press.

GHIZZO, A. & BERTRAND, P. 2013 On the multi-stream approach of relativistic Weibel instability. I, II and III. *Phys. Plasmas* **20** (8), 082109, 082110 and 082111.

GHIZZO, A., DEL SARTO, D. & RÉVEILLÉ, T. 2009 Hamiltonian stochastic processes induced by successive wave-particle interactions in stimulated Raman scattering. *Phys. Plasmas* **79** (4), 046404.

GHIZZO, A., DEL SARTO, D., RÉVEILLÉ, T., BESSE, N. & KLEIN, R. 2007 Self-induced transparency scenario revisited via beat-wave heating induced by Doppler shift in overdense plasma layer. *Phys. Plasmas* **14** (6), 062702.

GHIZZO, A., HUOT, F. & BERTRAND, P. 2003 A non-periodic 2D semi-Lagrangian Vlasov code for laser–plasma interaction on parallel computer. *J. Comput. Phys.* **186** (1), 47–69.

GHIZZO, A., JOHNSTON, T. W., RÉVEILLÉ, T., BERTRAND, P. & ALBRECHT-MARC, M. 2006 Stimulated-Raman-scatter behavior in a relativistically hot plasma slab and an electromagnetic low-order pseudocavity. *Phys. Rev.* E **74** (4), 046407.

GHIZZO, A., SARRAT, M. & DEL SARTO, D. 2016 Vlasov models for kinetic Weibel-type instabilities. *J. Plasma Phys.* **83** (1), doi:10.1017/S0022377816001215.

GHORBANALILU, M., SADEGZADEH, S., GHADERI, Z. & NIKNAM, A. R. 2014 Weibel instability for a streaming electron, counterstreaming e-e, and e-p plasmas with intrinsic temperature anisotropy. *Phys. Plasmas* **21** (5), 052102.

GUÉRIN, S., MORA, P., ADAM, J. C., HRON, A. & LAVAL, G. 1996 Propagation of ultraintense laser pulses through overdense plasma layers. *Phys. Plasmas* **3** (7), 2693–2701.

INGLEBERT, A., GHIZZO, A., RÉVEILLÉ, T., BERTRAND, P. & CALIFANO, F. 2012 Electron temperature anisotropy instabilities represented by superposition of streams. *Phys. Plasmas* **19** (12), 122109.

https://doi.org/10.1017/S0022377816001264 Published online by Cambridge University Press

INGLEBERT, A., GHIZZO, A., RÉVEILLÉ, T., DEL SARTO, D., BERTRAND, P. & CALIFANO, F. 2011 A multi-stream Vlasov modeling unifying relativistic Weibel-type instabilities. *Europhys. Lett.* **95** (4), 45002.

LAZAR, M. 2008 Fast magnetization in countestreaming plasmas with temperature anisotropies. *Phys. Lett.* A **372** (14), 2446–2449.

LAZAR, M., DIECKMANN, M. E. & POEDTS, S. 2010 Resonant Weibel instability in counterstreaming plasmas with temperature anisotropies. *J. Plasma Phys.* **76** (1), 49–56.

LAZAR, M., SCHLICKEISER, R. & SHUKLA, P. K. 2006 Cumulative effect of the filamentation and Weibel instabilities in countestreaming thermal plasmas. *Phys. Plasmas* **13** (10), 102107.

LAZAR, M., SCHLICKEISER, R., WIELEBINSKI, R. & POEDTS, S. 2009 Cosmological effects of Weibel-type instabilities. *Astrophys. J.* **693**, 1133–1141.

MASSON-LABORDE, P. E., ROZMUS, W., PENG, Z., PESME, D., HLLER, S., CASANOVA, M., BYCHENKOV, V. YU., CHAPMAN, T. & LOISEAU, P. 2010 Evolution of the stimulated Raman scattering instability in two-dimensional particle-in-cell simulations. *Phys. Plasmas* **17** (9), 092704.

MATTEINI, L., HELLINGER, P., LANDI, S., TRÁVNÍCEK, P. M. & VELLI, M. 2011 Ion kinetics in the solar wind: coupling global expansion to local microphysics. *Space Sci. Rev.* **172** (1–4), 373.

MEDVEDEV, M. V. & LOEB, A. 1999 Generation of magnetic fields in the relativistic shock of gamma-ray burst sources. *Astrophys. J.* **526** (2), 697.

PARASHAR, T. N. & MATTHAEUS, W. H. 2016 Propinquity of current and vortex structures: effects on collisionless plasma heating. *Astrophys. J.* **832**, 1, 57.

PEGORARO, F., BULANOV, S. V., CALIFANO, F. & LONTANO, M. 1996 Nonlinear development of the Weibel instability and magnetic field generation in collisionless plasmas. *Phys. Scripta* **T63**, 262.

SARRAT, M., DEL SARTO, D. & GHIZZO, A. 2016 Fluid description of Weibel-type instabilities via full pressure tensor dynamics. *Europhys. Lett.* **115** (4), 45001.

SCHLICKEISER, R. & SHUKLA, P. K. 2003 Cosmological magnetic field generation by the Weibel instability. *Astrophys. J.* **599**, L57–L60.

SCUDDER, J. D. 2016 Collisionless reconnection and electron demagnetization. In *Magnetic Reconnection*, pp. 33–100. Springer.

SCUDDER, J. D. & DAUGHTON, W. S. 2008 Illuminating electron diffusion regions of collisionless magnetic reconnection using electron agyrotropy. *J. Geophys. Res.* **113**, A6, 2156–2202.

SCUDDER, J. D., HOLDAWAY, R. D., DAUGHTON, W. S., KARIMABADI, H., ROYTERSHTEYN, V., RUSSELL, C. T. & LOPEZ, J. Y. 2012 First resolved observations of the demagnetized electron-diffusion region of an astrophysical magnetic-reconnection site. *Phys. Rev. Lett.* **108** (22), 225005.

SENTOKU, Y., MIMA, K., KAW, P. & NISHIKAWA, K. 2003 Anomalous resistivity resulting from MeV-electron transport in overdense plasma. *Phys. Rev. Lett.* **90** (15), 155001.

SERVIDIO, S., VALENTINI, F., CALIFANO, F. & VELTRI, P. 2012 Local kinetic effects in two-dimensional plasma turbulence. *Phys. Rev. Lett.* **108** (4), 045001.

SERVIDIO, S., VALENTINI, F., PERRONE, D., GRECO, A., CALIFANO, F., MATTHAEUS, W. H. & VELTRI, P. 2015 A kinetic model of plasma turbulence. *J. Plasma Phys.* **81** (1), 325810107.

STOCKEM, A. & LAZAR, M. 2008 Revision of 'cumulative effect of the filamentation and Weibel instabilities in countestreaming thermal plasmas'. *Phys. Plasmas* **15** (1), 014501.

STOCKEM, A., LAZAR, M., SHUKLA, P. K. & SMOLYAKOV, A. 2008 A comparative study of the filamentation and Weibel instabilities and their cumulative effect. II. Weakly relativistic beams. *J. Plasma Phys.* **75** (4), 529–543.

TZOUFRAS, M., REN, C., TSUNG, F. S., TONGE, J. W., MORI, W. B., FIORE, M., FONSECA, R. A. & SILVA, L. O. 2006 Space-charge effects in the current-filamentation or Weibel instability. *Phys. Rev. Lett.* **96** (10), 105002.

WEIBEL, E. S. 1959 Spontaneously growing transverse waves in a plasma due to an anisotropic velocity distribution. *Phys. Rev. Lett.* **2** (3), 83–84.

ZHENG, C. Y., HE, X. T. & ZHU, S. P. 2005 Magnetic field generation and relativistic electron dynamics in circularly polarized intense laser interaction with dense plasma. *Phys. Plasmas* **12** (4), 044505.

https://doi.org/10.1017/S0022377816001264 Published online by Cambridge University Press